Electrochimica Acta 210 (2016) 596–605

Contents lists available at ScienceDirect

Electrochimica Acta

journal homepage: www.elsevier.com/locate/electacta

Diagnosis of a cathode-supported solid oxide electrolysis cell by electrochemical impedance spectroscopy

Aziz Nechache[a,*], Aurore Mansuy[b], Marie Petitjean[b], Julie Mougin[b], Fabrice Mauvy[c], Bernard A. Boukamp[d], Michel Cassir[a,1], Armelle Ringuedé[*,a,1]

[a] PSL Research University – Chimie-ParisTech – CNRS, Institut de Recherche de Chimie Paris, 75005, Paris, France
[b] CEA-Grenoble, LITEN/DTBH, 17 rue des Martyrs, F-38054 Grenoble Cedex 9, France
[c] CNRS, Université de Bordeaux, ICMCB, 87, Av. du Dr Schweitzer, 33608 Pessac, France
[d] University of Twente, Dept. of Science and Technology & MESA Institute for Nanotechnology, P.O. Box 217, 7500 AE Enschede, The Netherlands

ARTICLE INFO

Article history:
Received 8 February 2016
Received in revised form 2 May 2016
Accepted 2 May 2016
Available online 18 May 2016

Keywords:
hydrogen
high temperature electrolysis
Solid Oxide Electrolysis Cell
electrochemical impedance spectroscopy
Distribution of relaxation times (DRT)
analysis of the difference in impedance spectra (ADIS)
reaction mechanisms

ABSTRACT

High-temperature electrolysis (HTSE) is a quite recent topic where most of the studies are focused on performance measurements and degradation observations, mainly achieved by polarization curve. However, it mainly leads to the overall cell behaviour. To get more specific knowledge on the operation of the cell, Electrochemical Impedance Spectroscopy (EIS) is more appropriate. In this study, EIS and chronopotentiometry were combined in order to characterize the electrochemical performance and behaviour of a commercial electrode-supported cell of Ni-YSZ/YSZ/LSCF type. A two-electrode configuration was used while a three-electrode one is required to better separate each component behavior. Nevertheless, it allows applying EIS to any single cell mainly when no good location for a reference electrode is available. Experimental parameters such as current density, temperature or P_{H2O}/P_{H2} ratio were analysed. Using electrical equivalent circuit (EEC) combined to the distribution of relaxation time (DRT) and the analysis of the difference in impedance spectra (ADIS) approaches allowed deconvoluting impedance diagrams into three or four arcs characterized by their specific capacitance and relaxation frequency. Each arc was ascribed to a phenomenon related to the electrochemical reactions. This work corresponds to an *in situ* diagnosis by EIS of solid oxide electrolyser cell reaction mechanisms.

1. Introduction

Our world is facing key issues such as always growing energy needs, mid-term disappearance of important energy resources such as fossil fuels and global warming consecutive to massive greenhouse effect. A possible answer to produce renewable and clean energy consists in combining promising technologies such as solar photovoltaic, wind turbine and fuel cell. Hydrogen can be part of this energy mix since it is considered as a leading candidate as energy carrier due to its clean, storable and transportable characteristics [1–3]. High temperature electrolysis (HTE) is a clean way to produce hydrogen from water and electricity. As shown in Fig. 1, HTE can be performed using a Solid Oxide Electrolysis Cell (SOEC) which is close to a reversibly operated Solid Oxide Fuel Cell (SOFC). Working at high temperature allows: (i) avoiding the use of expensive catalyst such as platinum, (ii) using less electrical energy balanced by more thermal energy which would be at least partly wasted otherwise, (iii) generating important quantities of directly pure hydrogen [1,2,4]. Thus, after one of the first studies on SOEC done by Dönitz through the HOTELLY project in the 1980's [4–6], interest in SOEC has strongly grown since the end of the 1990's [7–11]. However, even if performances can be improved by the operating temperature (>700 °C), degradation of the SOEC is enhanced as well. As recently reviewed [12], among recent studies focusing on SOEC [13–51], only few complete works are related to SOEC degradation [28–38], and even less using Electrochemical Impedance Spectroscopy (EIS) [39–51]. The others are more dedicated to performance measurements and characterizations [13–27]. Distribution of relaxation times (DRT) and the analysis of the difference in impedance spectra (ADIS) are two deconvolution methods that allow preventing any user subjectivity. Thus, DRT or ADIS analysis of an impedance diagram can be used as a pre-identification tool to select the

* Corresponding authors at: Research University – Chimie-ParisTech – CNRS, Institut de Recherche de Chimie Paris, 75005, Paris, France. Tel.: +33 155421235; fax: +33 144276750.
E-mail addresses: aziz.nechache@chimie-paristech.fr (A. Nechache), armelle.ringuede@chimie-paristech.fr (A. Ringuedé).
[1] ISE Member.

http://dx.doi.org/10.1016/j.electacta.2016.05.014
0013-4686/

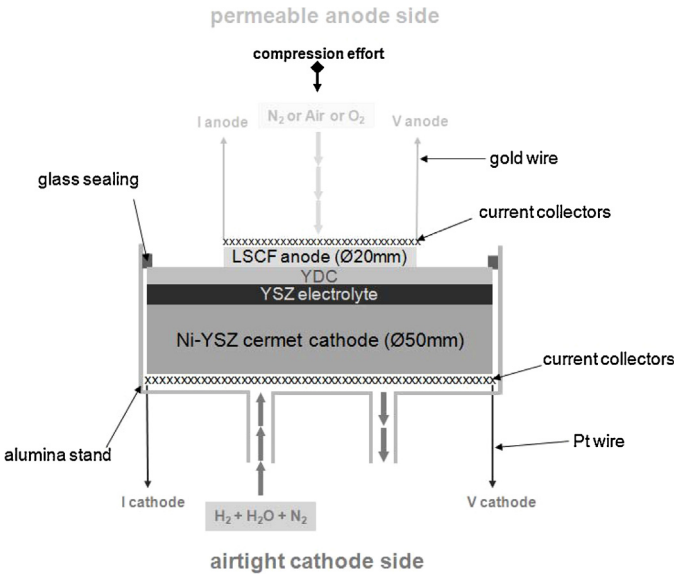

Fig. 1. Experimental set-up of the studied cell.

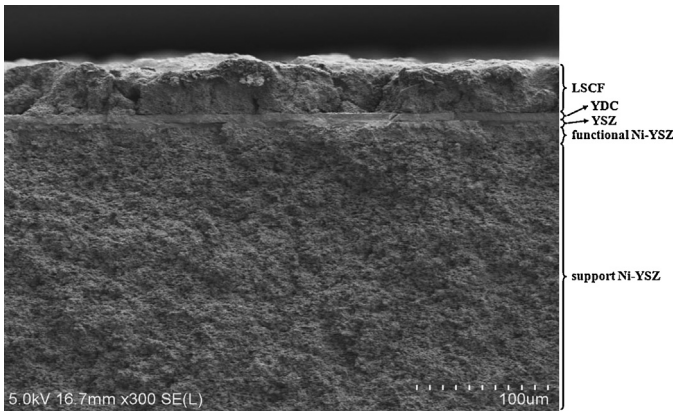

Fig. 2. SEM cross section image of the different layers constituting the cell before the test, as follows from top to bottom: Ni-YSZ electrode supporting layer, Ni-YSZ electrode functional layer, YSZ electrolyte, YDC intermediary layer, LSCF electrode.

electrical equivalent circuit (EEC) most adapted to the studied system. Consequently, the combined use of DRT (or ADIS) and EEC is strongly recommended to optimize an objective EIS analysis.

In this work, EIS and chronopotentiometry are combined to investigate the influence of several parameters such as current density, temperature, P_{H2O}/P_{H2} ratio and inlet H_2 electrode gas flow rate on the cell behavior. The use of an EEC combined with DRT and ADIS allows deconvoluting the measured impedance diagrams into several arcs, each arc associated to a capacitance and a relaxation frequency. Thus, each arc can be ascribed to a phenomenon directly related to the electrochemical reactions. This approach is developed in view of an *in situ* diagnosis tool of solid oxide electrolyser cell reaction mechanisms.

2. Experimental

Fig. 1 shows the two-electrode experimental set-up of the cell selected for this study, a LSCF//YSZ//Ni-YSZ commercial anode-supported SOFC used in HTSE mode (HC Starck). An intermediate YDC (Yttria-doped Ceria) layer is present between LSCF ($La_{0.6}Sr_{0.4}Co_{0.2}Fe_{0.8}O_{3-\delta}$) and YSZ (Yttria Stabilised Zirconia). A scanning electron microscopy (SEM) cross section image of the different layers constituting the cell before the test is shown Fig. 2. The circular cell has an active electrode area of 3.14 cm^2, based on the LSCF diameter (20 mm). Thus, considering the thin electrolyte (about 5 μm), this could mean that only part of Ni-YSZ is active, due to the current distribution. A compression effort of 20 N/cm^2 was exerted to the cell from the anode side. It is worth noting that a two-electrode configuration was used instead of a three-electrode one. Indeed, when studying actual cathode supported-cells, placement of an accurate and reliable reference electrode is impossible. Adding a reference electrode required then a specially designed cell which has no direct relation with a commercially available cell. Electrochemical Impedance Spectroscopy (EIS) and chronopotentiometry were combined to characterize the electrochemical performance and behavior of the cell by studying current density, temperature, P_{H2O}/P_{H2} ratio, H_2 electrode gas flow rate and H_2O/H_2 gas dilution with N_2. Table 1 contains the experimental conditions for each parameter considered. The electrochemical impedance diagrams were recorded applying a dc current with a

Table 1
Experimental conditions for each parameter considered in this study.

	Parameter considered	Values studied	experimental conditions				
			T, °C	P_{H2O}/P_{H2} (H_2 electrode)	O_2 electrode gas composition	H_2 electrode gas flow rate, NL/h	i, A/cm^2
Fig. 7	T, °C	650 700 800	–	9	N_2 air O_2	x 1*	−0.500
Fig. 8	P_{H2O}/P_{H2}	1 5 9	650	–	air	x 1*	−0.016 −0.064 −0.127 −0.350
Fig. 9	H_2 electrode gas flow rate, NL/h	x 1* x 1.5** x 2***	800	9	air	–	−0.016 −0.127 −0.446 −0.924
Fig. 10	P_{H2O}, atm (H_2O/H_2 gas dilution with N_2)	0.90 0.63 0.48	800	9	air	x 1*	−0.500
Fig. 11	i, A/cm^2	−0.016 −0.127 −0.318 −0.500 −0.730	800	9	air	x 1*	–

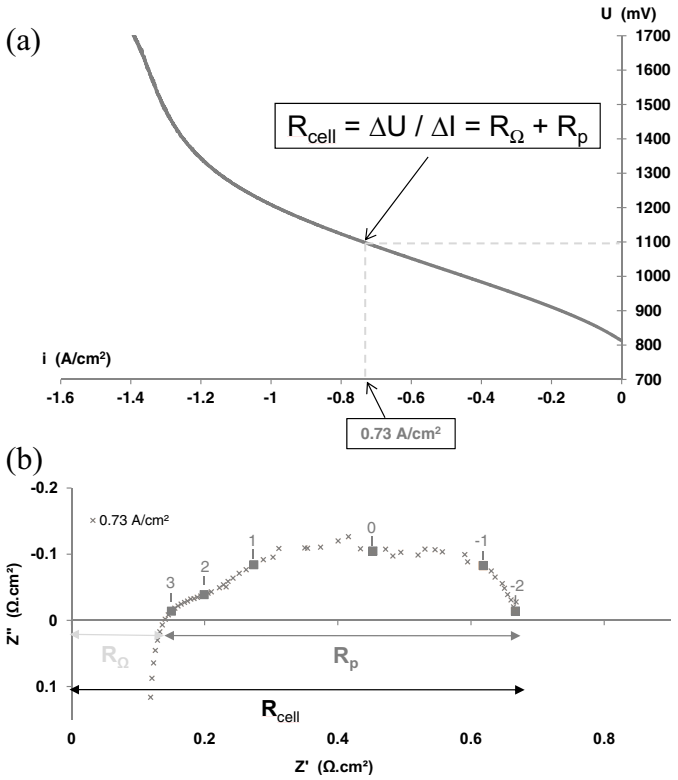

Fig. 3. Typical (a) i-U curve and (b) impedance diagram of the cell used in HTSE mode. T = 800 °C, P_{H2O}/P_{H2} = 9 (H_2 electrode), air (O_2 electrode), H_2 electrode gas flow rate of 2.26 NL/h.

30 mA amplitude perturbation in the frequency range from 10 kHz to 0.01 Hz with 10 points per decade. The current density-potential (i-U) curves were recorded in galvanostatic mode with a rate of 10 mA/s. An Autolab PGSTAT302 N frequency analyzer was used for both EIS and chronopotentiometry measurements.

3. Results and discussion

3.1. Polarisation resistance

To study the cell behavior, one may begin considering the polarization resistance (R_p) related to electrode mechanisms

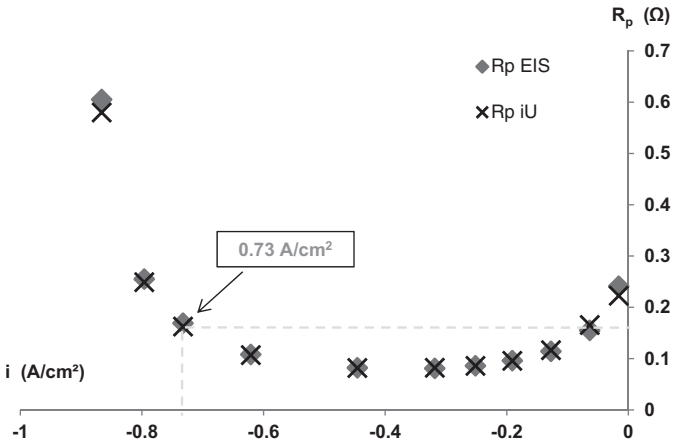

Fig. 4. Evolution of the polarization resistance Rp with current density. T = 800 °C, P_{H2O}/P_{H2} = 9 (H_2 electrode), air (O_2 electrode), H_2 electrode gas flow rate of 2.26 NL/h.

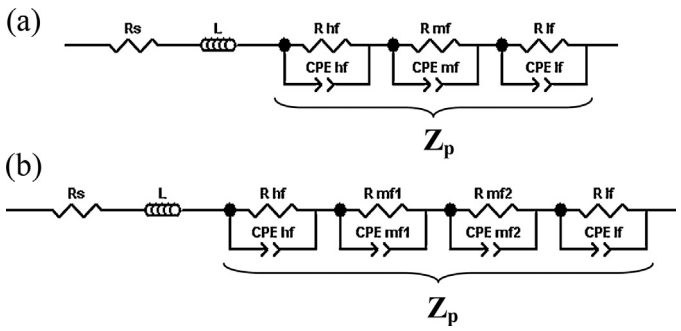

Fig. 5. Electrical equivalent circuits used in this study with L in series with Rs and in series with Zp constituted of three (a) or four (b) circuits of a resistance in parallel with a constant phase element.

occurring while the cell is in use. Only the total cell resistance R_{cell} can be calculated directly from the slope of the i-U curve, at each i-U point. R_{cell} includes the ohmic resistance (R_Ω) and the polarization resistance (R_p) (Fig. 3a). The use of impedance spectroscopy allows to separate them as illustrated in Fig. 3b. Thus, R_p is calculated as $R_p = R_{cell}-R_\Omega$ using in both cases (from EIS or I-U diagrams) R_Ω values determined from the high frequency intercept of the diagram and the x-axis of the Nyquist diagram (real part of impedance, Z'). As reported in Fig. 4, plotting R_p for different current densities leads, in this study, to a "basin-like" evolution of R_p with three regions: a first region where R_p decreases with increasing current densities corresponding to a decrease in the activation resistance, a second region where R_p reaches a minimum

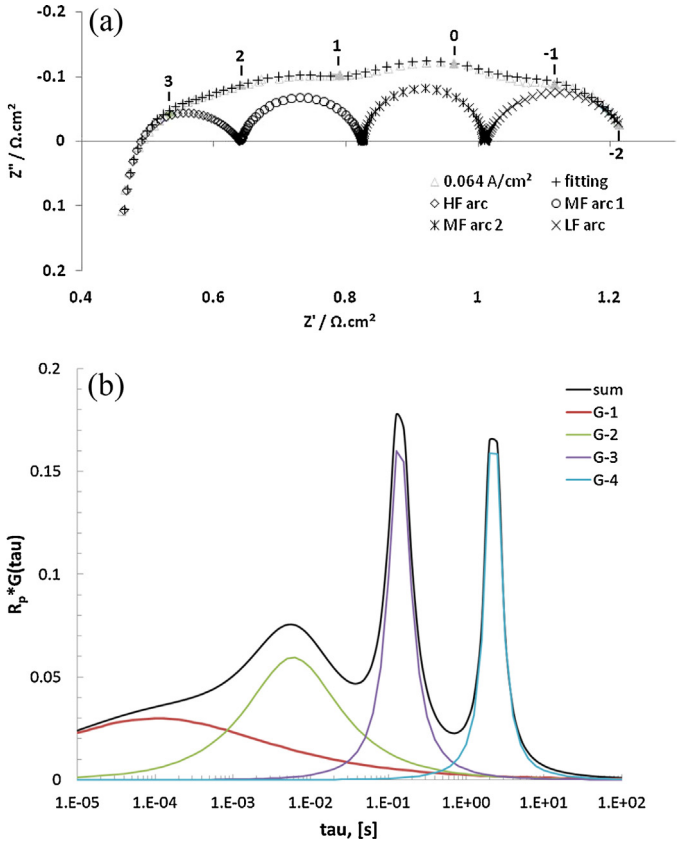

Fig. 6. Example of a fitting done on an impedance diagram (a) using Fig. 5b. In this example, the EEC was selected after the use of DRT (b). i = −0.064 A/cm², T = 650 °C, P_{H2O}/P_{H2} = 9 (H_2 electrode), air (O_2 electrode), H_2 electrode gas flow rate of 2.26 NL/h.

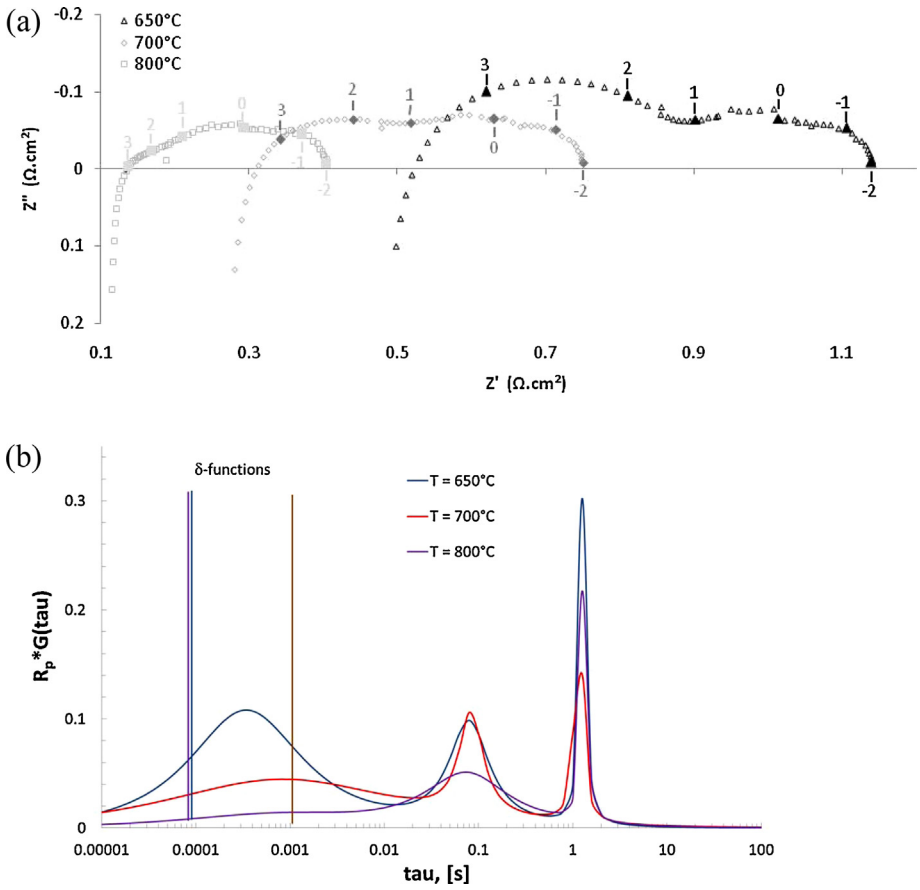

Fig. 7. (a) Impedance diagram measured at different temperatures (650 °C, 700 °C and 800 °C). i = −0.5 A/cm^2, P_{H2O}/P_{H2} = 9 (H_2 electrode), air (O_2 electrode), H_2 electrode gas flow rate of 2.26 NL/h; (b) DRT-representation obtained for the different temperatures.

and remains constant while current density increases showing an optimal use of the cell, and a third region where R_p increases with current density resulting mainly from an increase of concentration overpotentials. Besides, a correlation between the i-U curve and the impedance diagram is obtained, with a standard deviation smaller than 8%.

3.2. Electrochemical Impedance Spectroscopy parameters

The impedance diagrams measured can be analysed by using Electrical Equivalent Circuit (EEC). Indeed, the association of the studied cell to an EEC allows relating each phenomenon occurring while the cell is in use to simple electrical elements such as resistance, capacitance or inductance (depending on the phenomena, mainly specific diffusion mechanisms, more complex component such as Warburg or Gerischer element could be considered for deeper analysis). Thus, by analysing and understanding the evolution of the behavior of the electrical element with the change of one parameter such as temperature or P_{H2O}/P_{H2} ratio for instance, one may deduce its influence on the reaction mechanism and the value of the electrical element becomes characteristic of the phenomenon. The extension of the experiments to different kind of cells (composition, microstructure, dimension, . . .) or/and as function of time can lead to the set-up of a data base for the identification of the main phenomena occurring in a SOEC in use, either at short or long term. Thus, this approach constitutes the frame of a systematic *in situ* diagnosis of the SOEC reaction mechanisms.

In our case, the EEC consists of an inductance (L) in series with the ohmic resistance R_Ω (or series R_s) and in series with the polarization impedance (Z_p). Depending on the impedance diagram considered, Z_p is constituted of three or four contributions, equivalent to 3 or 4 R and CPE (Constant Phase Element) parallel combinations as represented in Fig. 5. Impedance diagram data analysis was done with ZView Software (Scribner). It should be noticed that even though the impedance diagrams recorded showed an inductance at higher frequencies, no significant difference was observed between R_Ω values, determined from the high frequency intercept of the diagram and Z', and the ones obtained from the fitting of the EEC, with a standard deviation always below 4%. To discriminate the co-existence of 3 or 4 contributions, DRT (and sometimes ADIS) analysis were performed as well for every parameter considered in this study, but not systematically shown. However, some representations are joined to the Nyquist impedance diagrams. Fig. 6 shows an example of a fitting done on an impedance diagram (Fig. 6a) using Fig. 5b. In this example, the EEC was selected after the use of DRT (Fig. 6b). Kramers-Krönig tests were performed in order to validate the consistency of the measured data (see details in Appendix, from Fig. A1 to A4). The DRT methodology adopted in this study is further explained elsewhere [52].

Several parameters were varied and their influence on the cell behavior studied using EIS in order to have a better understanding on the phenomena governing the cell while it is in use.

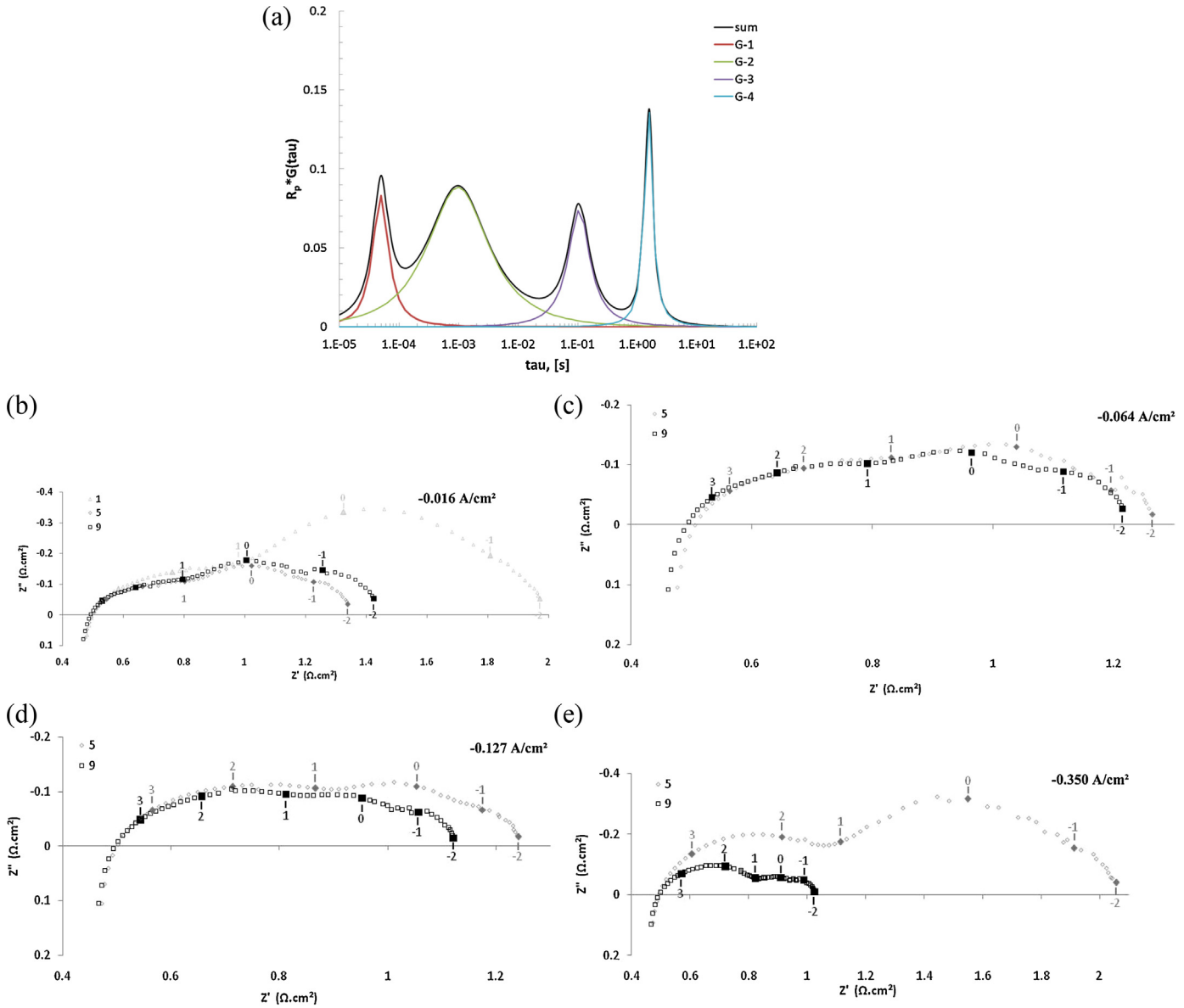

Fig. 8. Influence of P_{H2O}/P_{H2} ratio on the impedance diagrams measured for different current densities (0.016 A/cm^2, 0.064 A/cm^2, 0.127 A/cm^2 and 0.350 A/cm^2 for b, c, d and e, respectively). T = 650 °C, air (O_2 electrode), H_2 electrode gas flow rate of 2.26 NL/h. Fig. 8a shows the DRT-representation obtained for i = −0.350 A/cm^2.

3.2.1. Temperature

As shown in Fig. 7, three temperatures were considered: 650 °C, 700 °C and 800 °C. The Nyquist impedance diagrams obtained here (Fig. 7a) can be deconvoluted into three arcs: a high frequency arc (HF arc), a middle frequency arc (MF arc) and a low frequency arc (LF arc); e.g. for the impedance diagram at 650 °C, the HF arc is located in a frequency range of 10 kHz to 20 Hz, the MF arc from 20 to 1 Hz and the LF arc from 1 to 0.01 Hz. This is confirmed by DRT analysis, as reported for all three temperatures in Fig. 7b. It is clear that HF arc evolves with the temperature while both MF and LF arcs remain almost unchanged. Indeed, the increase in temperature leads to a significant decrease in HF arc resistance, which means that it is thermally activated. This is confirmed by activation energy of 0.79 eV obtained for HF arc while 0.08 eV and 0.10 eV were calculated for MF and LF arcs, respectively. Thus, it is relevant to relate the HF arc to charge transfer at the electrode/electrolyte interface [53–57] since this phenomenon is thermally activated. Unfortunately, at this stage of the study, it is not possible to distinguish the cathode and anode charge transfers.

3.2.2. P_{H2O}/P_{H2} ratio at the H_2 electrode

Fig. 8 shows the effect of P_{H2O}/P_{H2} ratio variation at different current densities and at T = 650 °C. In this case, the impedance diagram measured can be deconvoluted into four arcs: a high frequency arc (HF arc), a first middle frequency arc (MF1 arc), a second middle frequency arc (MF2 arc) and a low frequency arc (LF arc). The deconvolution in four arcs is confirmed by DRT analysis, as reported in Fig. 8a. For low current densities applied (Fig. 8b), increasing the P_{H2O}/P_{H2} ratio from 1 to 5 leads to an important decrease in the four arcs amplitude while increasing this ratio from 5 to 9 leads only to the decrease in MF2 and LF arcs. For higher current densities applied (Fig. 8c and d), the increase in the ratio still leads to the decrease in MF2 and LF arcs amplitude while HF and MF1 arcs remain unchanged. From −0.350 A/cm^2 applied

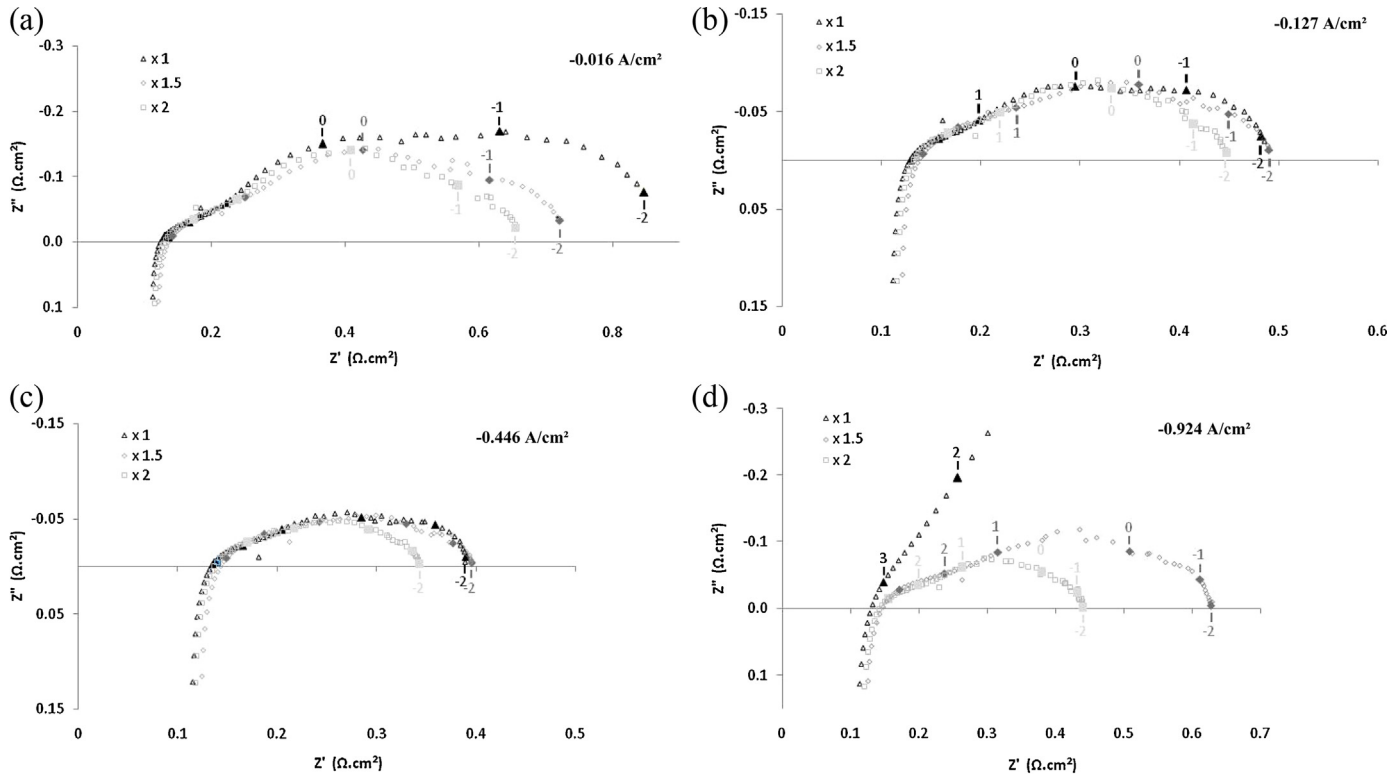

Fig. 9. Influence of H_2 electrode gas flow rate on the impedance diagrams measured for different current densities (0.016 A/cm^2, 0.127 A/cm^2, 0.446 A/cm^2 and 0.924 A/cm^2 for a, b, c and d, respectively). The indications ×1, ×1.5 and ×2 correspond to 2.26 NL/h, 3.39 NL/h and 4.52 NL/h, respectively. T = 800 °C, P_{H2O}/P_{H2} = 9 (H_2 electrode), air (O_2 electrode).

(Fig. 8e), a ratio increase leads again to a decrease in all the arcs but, in particular, MF2 and LF arcs. Thus, increasing P_{H2O}/P_{H2} ratio leads mostly to a decrease in MF2 arc, which might be associated to gas conversion at the H_2 electrode [58,59], and LF arc widely associated to gas diffusion at the Ni-YSZ electrode [53,60–62].

3.2.3. Gas flow rate at the H_2 electrode

Fig. 9 shows the effect of inlet gas flow rate at the H_2 electrode side on the cell behaviour. In this case, the impedance diagram can be deconvoluted into three or four arcs, depending on the applied current density. The impedance diagrams measured are influenced in two different ways by the change in this parameter. First, increasing the cathode gas flow rate leads to a decrease in MF and LF regions of the diagram for all the applied current densities but more significantly for the lowest and the highest studied current densities (Fig. 9a and d). This strengthens the previous association of the MF region to gas conversion at the H_2 electrode and the LF region to gas diffusion at the H_2 electrode. Moreover, increasing the gas flow rate by half leads to a shift of the frequencies to the lower part of the diagram even if the overall diagram remains the same in terms of R_s and R_p values (Fig. 9b and c). This probably means that increasing the gas flow rate leads at the same time to a more efficient gas diffusion and gas conversion at the H_2 electrode characterized by a decrease in the associated resistances and a slower charge transfer at the cathode/electrolyte interface characterized by an increase in the related resistance. Nevertheless, further investigation is surely needed.

3.2.4. H_2O/H_2 dilution with N_2

The principle of this parameter consists in adding different amounts of N_2 gas to the H_2O/H_2 gas supplied at the H_2 electrode, always for the same ratio P_{H2O}/P_{H2} = 9. The different N_2 quantities added leads to PH_2O = 0.90, 0.63 and 0.48 atm. Fig. 10 represents the impedance diagram measured for the different PH_2O (Fig. 10a) and the differential diagram obtained by ADIS for the dilution ratios 0.90/0.63 and 0.90/0.48 (Fig. 10b). In this case, according to the differential diagram Fig. 10b, the impedance diagram can be deconvoluted into four arcs. Increasing dilution of H_2O/H_2 gas with N_2 leads to an important increase of the MF1 and MF2 arcs, with f_{MF1} = 11 Hz and f_{MF2} = 2 Hz. This once again strengthens the association of the MF1 arc to gas diffusion at the H_2 electrode and the MF2 to gas conversion at the H_2 electrode [54,59,60].

3.2.5. Current density

The influence of current density was then considered. The following discussed trends were the same for the three considered temperatures (650 °C, 700 °C, 800 °C). Thus, only measurements made at 800 °C are shown here. In this case, the impedance diagram can be deconvoluted into three arcs. As seen from Fig. 11, increasing current density first leads to an overall decrease in the total resistance (low frequency intercept with the real axis), which according to the previous discussions means a faster charge transfer at the Ni-YSZ/YSZ interface, an easier O^{2-} ions transport at the O_2 electrode and/or a more efficient gas conversion at the H_2 electrode, and a better gas supply at the H_2 electrode. Then, all these phenomena governing the cell are optimised when the current density reaches ~−0.5 A/cm^2. In an opposite way, increasing current density above this value increases the values of impedance which is most probably due to lower rates of the mentioned phenomena.

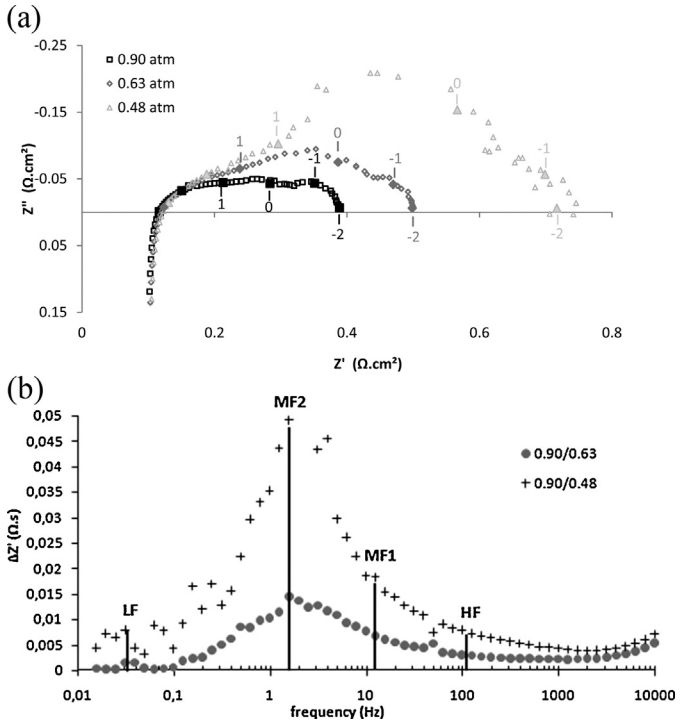

Fig. 10. (a) Influence of the dilution of the H_2O/H_2 gas with N_2 on the impedance diagrams measured and (b) ADIS diagram of the P_{H2O} ratios 0.90/0.63 and 0.90/0.48. i = −0.500 A/cm², T = 800 °C, P_{H2O}/P_{H2} = 9 (H2 electrode), air (O_2 electrode), H_2 electrode gas flow rate of 2.26 NL/h.

3.3. Impedance diagram analysis using EEC

Table 2 summarizes the values of capacitance (C) and relaxation frequency (f) obtained for each of the studied parameters, using the formula:

$$C = \sqrt[n]{R \cdot Y_0}\overline{R} \quad (1)$$

$$f = \frac{1}{2\pi \sqrt[n]{R \cdot Y_0}} \quad (2)$$

where Y_0 and n are CPE parameters. R is the resistance of the corresponding phenomenon.

The orders of magnitude relative to these parameters for the high frequency {C_{HF} = 1 mF/cm², f_{HF} = [100 Hz–1000 Hz]} and low frequency arcs {C_{LF} = 10 F/cm², f_{LF} = 0.1 Hz} confirm that they are mainly associated to charge transfer at the cathode/electrolyte interface and gas diffusion at the Ni-YSZ electrode, respectively. Indeed, for both arcs: (i) it is relevant to associate the obtained values to the suggested phenomena, (ii) these values are in agreement with the literature [53,54,60–66]. The middle frequency part of the impedance diagram is constituted by one or two arcs, depending on the experimental conditions of the cell test. The corresponding capacitance and relaxation frequency orders of magnitude are C_{MF} = 0.1 F/cm², f_{MF} = 1 Hz when one arc is considered, and C_{MF1} = 0.1 F/cm², f_{MF1} = 10 Hz; C_{MF2} = 0.5 F/cm², f_{MF2} = 1 Hz when two arcs are considered. According to the discussion above (see part 3.2) and the literature, these values might rather be ascribed to gas diffusion at the H_2 electrode for MF1 and gas conversion at the H_2 electrode for MF2 [54,59,60,67–70], even if we can not exclude at this stage gas diffusion at the O_2 electrode [71] and/or O^{2-} ion transport through the O_2 electrode [71]. An

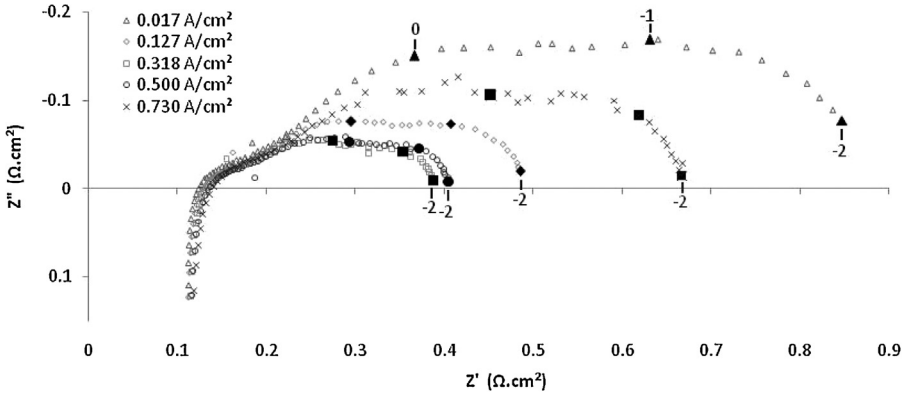

Fig. 11. Impedance diagram measured for different current densities (0.017 A/cm², 0.127 A/cm², 0.318 A/cm², 0.500 A/cm² and 0.730 A/cm²). T = 800 °C, P_{H2O}/P_{H2} = 9 (H_2 electrode), air (O_2 electrode), H_2 electrode gas flow rate of 2.26 NL/h.

Table 2
Summary of the values obtained applying EECs to the impedance diagrams of this study, except figure 10 (see Table 1 for experimental details).

		C_{HF} (F/cm^2)	C_{MF2} (F/cm^2)			f_{HF} (Hz)	f_{MF} (Hz)		f_{LF} (Hz)
			C_{MF1} (F/cm^2)	C_{MF} (F/cm^2)			f_{MF1} (Hz)	f_{MF2} (Hz)	
Fig. 7	650 °C	0.003		0.35	11	400		3.0	0.17
	700 °C	0.001		0.34	9	400		3.0	0.17
	800 °C	0.002		0.41	13	450		2.5	0.15
Fig. 8	0.016 A/cm^2	0.001	0.02	0.27	10	800	53	1.1	0.08
	0.064 A/cm^2	0.001	0.03	0.48	9	940	32	1.6	0.11
	0.127 A/cm^2	0.001	0.22	0.32	9	860	43	2.2	0.14
	0.350 A/cm^2	0.001		0.40	8	320		1.7	0.18
Fig. 9 (with not shown values)	0.016 A/cm^2	0.007	0.16	0.53	12	290	21	1.0	0.07
	0.064 A/cm^2	0.010	0.10	0.66	17	300	24	1.2	0.08
	0.127 A/cm^2	0.008		0.50	18	210		1.7	0.12
	0.446 A/cm^2	0.005		0.35	17	400		4.0	0.19
	0.924 A/cm^2	0.004		0.16	3	500		5.0	0.55
	1.210 A/cm^2	0.004		0.04	2	270		4.0	0.43
Fig. 11	0.017 A/cm^2	0.020		0.65	9	62		0.8	0.05
	0.127 A/cm^2	0.020		0.78	9	93		1.6	0.10
	0.318 A/cm^2	0.010		0.72	14	136		2.1	0.13
	0.500 A/cm^2	0.009		0.53	11	202		2.7	0.15
	0.732 A/cm^2	0.006		0.26	9	177		2.2	0.13
Order of magnitude		**1 mF/cm^2**		**0.1 F/cm^2**	**10 F/cm^2**	**100 Hz**		**1 Hz**	**0.1 Hz**
			0.1 F/cm^2	**0.5 F/cm^2**			**10 Hz**	**1 Hz**	

additional study on the same commercial cell showed that all the main phenomena governing the cell functioning are associated to the cathode side [72,73]. Consequently, MF1 and MF2 can be clearly ascribed to gas diffusion and gas conversion at the H_2 electrode, respectively.

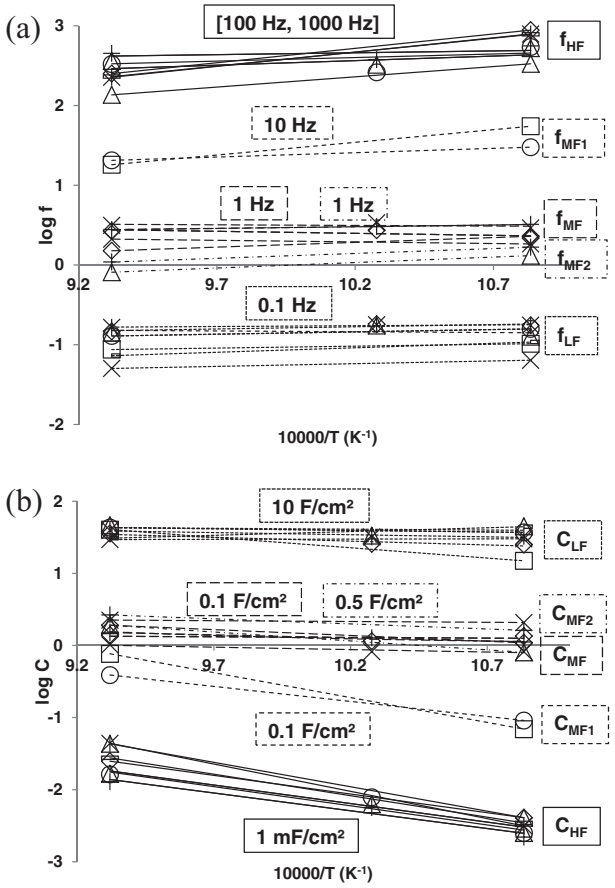

Fig. 12. Arrhenius plots showing orders of magnitude for(a) relaxation frequency and (b) capacitance obtained through this study. $P_{H2O}/P_{H2} = 9$ (H_2 electrode), air (O_2 electrode), H_2 electrode gas flow rate of 2.26 NL/h.

It is furthermore interesting to deduce from Fig. 12a and b that the phenomena influencing the studied cell are characterized by capacitances and relaxation frequencies with different orders of magnitude, meaning that applying this approach clearly allows distinguishing the main phenomena governing the SOEC, at short term in this case. Thus, it would surely be useful applying this methodology to a long term study to have a better understanding of the specific phenomena and mechanisms responsible of SOEC degradation. It should be pointed out that no significant degradation of the cell was observed during this study. This aspect however was not the aim of this work, for which stability of the cell behaviour was of primary importance to ensure reliability of the approach developed here. Nevertheless, the statements made throughout this study can be significantly useful for the understanding of cell degradation behaviour in electrolysis mode. Hence, a degradation study of a similar cell using the conclusions of this paper is under publication process [73].

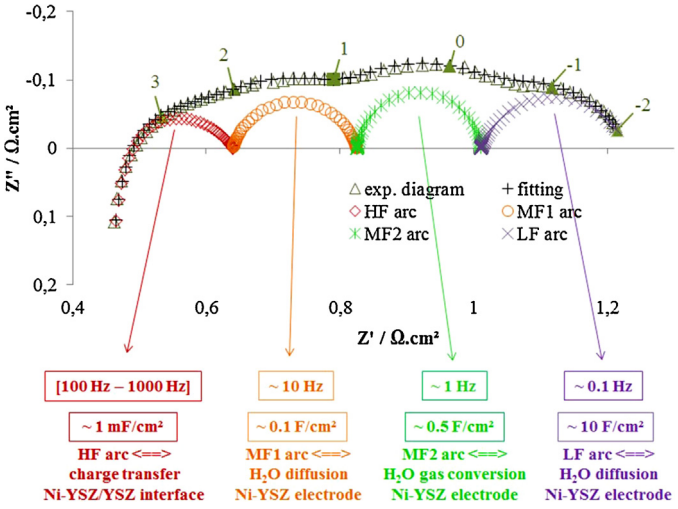

Fig. 13. Illustration summarizing the main impedance diagram contributions identified (in the case of four arcs) with relaxation frequency and capacitance orders of magnitude, and the associated phenomena.

Deeper quantitative evaluation of the cell could be performed, including: (i) analysis of the evolution of the relaxation frequency, the capacitance and the resistance associated with the main processes identified here, (ii) calculation and discussion of the activation energy for each process. This quantitative aspect might be further considered in upcoming studies.

4. Conclusions

The electrochemical behavior of a commercial electrode supported cell was studied in electrolysis mode through the combination of EIS and polarisation curve. The polarization resistance of the cell was first considered and showed a "basin-like" evolution with increasing current densities. Several parameters were then investigated and, with the use of EEC, impedance diagrams were deconvoluted into several arcs, each arc associated to a capacitance and a relaxation frequency. HF and LF arcs were clearly identified: the HF arc characterized by $C_{HF} \approx 1\,mF/cm^2$ and $f_{HF} \approx [100\,Hz–1000\,Hz]$ is associated to charge transfer at the cathode/electrolyte interface and the LF arc characterized by $C_{LF} \approx 10\,F/cm^2$ and $f_{LF} \approx 0.1\,Hz$ to gas diffusion at the Ni-YSZ electrode. The middle frequency part of the impedance diagram is constituted by one or two arcs, depending on the experimental conditions of the cell. The corresponding capacitance and relaxation frequency orders of magnitude are $C_{MF} = 0.1\,F/cm^2$, $f_{MF} = 1\,Hz$ when one arc is considered, and $C_{MF1} = 0.1\,F/cm^2$, $f_{MF1} = 10\,Hz$; $C_{MF2} = 0.5\,F/cm^2$, $f_{MF2} = 1\,Hz$ when two arcs are considered. These values can be ascribed to gas diffusion at the H_2 electrode for MF1 and gas conversion at the H_2 electrode for MF2. These conclusions are summarized in Fig. 13. In the near future, this approach developed in view of an *in situ* diagnosis tool of SOEC reaction mechanisms and degradation will be applied to other single cells with new electrode materials (whatever the electrochemical configuration and architecture) and extended to single repeat units (SRU), and stacks.

Acknowledgements

This work is supported by the French Research National Agency (ANR) through *Hydrogène et piles à combustible* program (project FIDELHYO n°ANR-09-HPAC-005).

The authors would like to thank Gilles Piat and Pascal Giroud for their technical expertise, and Jérôme Laurencin for helpful discussion.

Appendix A. Supplementary data

Supplementary data associated with this article can be found, in the online version, at http://dx.doi.org/10.1016/j.electacta.2016.05.014.

References

[1] M.A. Laguna-Bercero, J. Power Sources 203 (2012) 4–16.
[2] National Academy of Sciences, National Research Council. The hydrogen economy: opportunities, costs, barriers, and R&D needs, February 2004.
[3] M.N. Manage, D. Hodgson, N. Milligan, S.J.R. Simons, D.J.L. Brett, Int. J. Hydrogen Energy 36 (2011) 5782–5796.
[4] W. Dönitz, R. Schmidberger, E. Steinheil, Int. J. Hydrogen Energy 5 (1980) 55–63.
[5] W. Dönitz, R. Schmidberger, Int. J. Hydrogen Energy 7 (1982) 321–330.
[6] W. Dönitz, E. Erdle, Int. J. Hydrogen Energy 10 (1985) 291–295.
[7] K. Eguchi, T. Hatagishi, H. Arai, Solid State Ionics 86–88 (1996) 1245–1249.
[8] A. Momma, T. Kato, Y. Kaga, S. Nagata, J. Ceram. Soc. Jpn 105 (1997) 369–373.
[9] K.V. Jensen, R. Wallenberg, I. Chorkendorff, M. Mogensen, Solid State Ionics 160 (2003) 27–37.
[10] R. Hino, K. Haga, H. Aita, K. Sekita, Nucl. Eng. Des. 233 (2004) 363–375.
[11] N. Osada, H. Uchida, M. Watanabe, J. Electrochem. Soc. 153 (2006) A816–A820.
[12] A. Nechache, M. Cassir, A. Ringuedé, J. Power Sources 258 (2014) 164–181.
[13] F. He, D. Song, R. Peng, G. Meng, S. Yang, J. Power Sources 195 (2010) 3359–3364.
[14] S.H. Jensen, X. Sun, S.D. Ebbesen, R. Knibbe, M. Mogensen, Int J. Hydrogen Energy 18 (2010) 9544–9549.
[15] A. Hauch, M. Mogensen, Solid State Ionics 181 (2010) 745–753.
[16] D. Grondin, J. Deseure, A. Brisse, M. Zahid, B. Grondin-Pérez, J.P. Chabriat, P. Ozil, ECS Trans. 35 (2011) 987–995.
[17] C. Bernuy-Lopez, R. Knibbe, Z. He, X. Mao, A. Hauch, K.A. Nielsen, J. Power Sources 196 (2011) 4396–4403.
[18] P. Kim-Lohsoontorn, J. Bae, J. Power Sources 196 (2011) 7161–7168.
[19] P.K. Patro, T. Delahaye, E. Bouyer, P.K. Sinha, Int. J. Hydrogen Energy 37 (2012) 3865–3873.
[20] F. Chauveau, J. Mougin, J.M. Bassat, F. Mauvy, J.C. Grenier, J. Power Sources 195 (2010) 744–749.
[21] T. Ogier, F. Chauveau, J.M. Bassat, F. Mauvy, J.C. Grenier, J. Mougin, M. Petitjean, ECS Trans. 35 (2011) 1817–1822.
[22] F. Lefebvre-Joud, M. Petitjean, J.P. Ouweltjes, A. Brisse, J. Bowen, J.U. Nielsen, Proceedings of the European Solid Oxide Fuel Cell Forum, Luzern, 2010.
[23] J. Laurencin, D. Kane, G. Delette, J. Deseure, F. Lefebvre-Joud, J. Power Sources 196 (2011) 2080–2093.
[24] S. Gopalan, M. Mosleh, J.J. Hartvigsen, R.D. McConnell, J. Power Sources 185 (2008) 1328–1333.
[25] T. Chen, M. Liu, C. Yuan, Y. Zhou, X. Ye, Z. Zhan, C. Xia, S. Wang, J. Power Sources 276 (2015) 1–6.
[26] Y. Wang, T. Liu, S. Fang, F. Chen, J. Power Sources 305 (2016) 240–248.
[27] E.-C. Shin, J. Ma, P.-A. Ahn, H.-H. Seo, D.T. Nguyen, J.S. Lee, Electrochim. Acta 188 (2016) 240–253.
[28] M. Keane, M.K. Mahapatra, A. Verma, P. Singh, Int. J. Hydrogen Energy 37 (2012) 16776–16785.
[29] M.S. Sohal, J.E. O'Brien, C.M. Stoots, V.I. Sharma, B. Yildiz, A. Virkar, Proceedings of the ASME Fuel Cell (2010) 1–11.
[30] J. Schefold, A. Brisse, M. Zahid, ECS Trans. 25 (2009) 1021–1028.
[31] J. Schefold, A. Brisse, M. Zahid, ECS Trans. 28 (2010) 357–367.
[32] S. Elangovan, J. Hartvigsen, D. Larsen, I. Bay, F. Zhao, ECS Trans. 35 (2011) 2875–2882.
[33] A.V. Virkar, Int. J. Hydrogen Energy 35 (2010) 9527–9543.
[34] C. Xu, Y. Wang, L. Jin, J. Ding, X. Ma, W.G. Wang, ECS Trans. 41 (2012) 97–102.
[35] V.I. Sharma, V. Yildiz, J. Electrochem. Soc. 157 (2010) B441–B448.
[36] J.R. Mawdsley, J.D. Carter, A.J. Kropf, B. Yildiz, V.A. Maroni, Int. J. Hydrogen Energy 34 (2009) 4198–4207.
[37] A. Mansuy, M. Petitjean, J. Mougin, F. Mauvy, Fundamentals and Developments of Fuel Cells Conference, Grenoble, 2011.
[38] G. Corre, A. Brisse, ECS Trans. 68 (2010) 3481–3490.
[39] A. Hauch, S.H. Jensen, M. Mogensen, J.B. Bilde-Sørensen, J. Electrochem. Soc. 154 (2007) A619–A626.
[40] F. Petipas, Q. Fu, A. Brisse, C. Bouallou, Int. J. Hydrogen Energy 38 (2013) 2957–2964.
[41] A. Ringuedé, S. Awamat, M. Cassir, L. Dessemond, S. Tadokoro, E. Lay, C. Steil, R. Laucournet, K. Couturier, Fundamentals and Developments of Fuel Cells Conference, Grenoble, 2011.
[42] G. Schiller, A. Ansar, M. Lang, O. Patz, J. Appl. Electrochem. 39 (2009) 293–301.
[43] K. Chen, N. Ai, S.P. Jiang, Int. J. Hydrogen Energy 37 (2012) 10517–10525.
[44] S.D. Ebbesen, C. Graves, A. Hauch, S.H. Jensen, M. Mogensen, J. Electrochem. Soc. 157 (2010) B1419–B1429.
[45] J. Schefold, A. Brisse, F. Tietz, J. Electrochem. Soc. 159 (2012) A137–A144.
[46] X. Sun, M. Chen, P. Hjalmarsson, S.D. Ebbesen, S.H. Jensen, M. Mogensen, P.V. Hendriksen, ECS Trans. 41 (2012) 77–85.
[47] M. Petitjean, M. Reytier, A. Chatroux, L. Bruguière, A. Mansuy, H. Sassoulas, S. Di Iorio, B. Morel, J. Mougin, ECS Trans. 35 (2011) 2905–2913.
[48] J. Schefold, A. Brisse, H. Poepke, Electrochim. Acta 179 (2015) 161–168.
[49] Q. Fang, L. Blum, N.H. Menzler, J. Electrochem. Soc. 162 (2015) F907–F912.
[50] J.-C. Njodzefon, D. Klotz, A. Kromp, A. Weber, E. Ivers-Tiffée, J. Electrochem. Soc. 160 (2013) F313–F323.
[51] K. Chen, J. Hyodo, N. Ai, T. Ishihara, S.P. Jiang, Int. J. Hydrogen Energy 41 (2016) 1419–1431.
[52] B.A. Boukamp, Electrochim. Acta 154 (2015) 35–46.
[53] A. Brisse, J. Schefold, M. Zahid, Int. J. Hydrogen Energy 33 (2008) 5375–5382.
[54] A. Leonide, V. Sonn, A. Weber, E. Ivers-Tiffée, J. Electrochem. Soc. 155 (2008) B36–B41.
[55] H.P. Dasari, S.Y. Park, J. Kim, J.H. Lee, B.K. Kim, H.J. Je, H.W. Lee, K.J. Yoon, J. Power Sources 240 (2013) 721–728.
[56] H. Fan, M. Keane, P. Singh, M. Han, J. Power Sources 268 (2014) 634–639.
[57] A.R. Hanifi, M.A. Laguna-Bercero, T.H. Etsell, P. Sarkar, Int. J. Hydrogen Energy 39 (2014) 8002–8008.
[58] C. Graves, S.D. Ebbesen, M. Mogensen, Solid State Ionics 192 (2011) 398–403.
[59] W. Wang, Y. Huang, S. Jung, J.M. Vohs, R.J. Gorte, J. Electrochem. Soc. 153 (2006) A2066–A2070.
[60] J. Schefold, A. Brisse, M. Zahid, J. Electrochem. Soc. 156 (2009) B897–B904.
[61] M.A. Laguna-Bercero, R. Campana, A. Larrea, J.A. Kilner, V.M. Orera, J. Power Sources 196 (2011) 8942–8947.
[62] S. Chen, K. Xie, D. Dong, H. Li, Q. Qin, Y. Zhang, Y. Wu, J. Power Sources 274 (2015) 718–729.
[63] J. Schefold, M.J. Garcia, A. Brisse, D. Perednis, M. Zahid, Proceedings of the 8th European SOFC Forum (2008) A1011.
[64] S.P. Jiang, S.P.S. Badwal, Solid State Ionics 123 (1999) 209–224.

[65] M.A. Laguna-Bercero, J.A. Kilner, S.J. Skinner, Chem. Mater. 22 (2010) 1134–1141.
[66] P. Hjalmarsson, X. Sun, Y.L. Liu, M. Chen, J. Power Sources 223 (2013) 349–357.
[67] A. Hauch, S.D. Ebbesen, S.H. Jensen, M. Mogensen, J. Electrochem. Soc. 155 (2008) B1184–B1193.
[68] R. Knibbe, M.L. Traulsen, A. Hauch, S.D. Ebbesen, M. Mogensen, J. Electrochem. Soc. 157 (2010) B1209–B1217.
[69] A. Hauch, S.H. Jensen, S. Ramousse, M. Mogensen, J. Electrochem. Soc. 153 (2006) A1741–A1747.
[70] S. Primdahl, M. Mogensen, J. Electrochem. Soc. 145 (1998) 2431–2438.
[71] M.J. Jorgensen, M. Mogensen, J. Electrochem. Soc. 148 (2001) A433–A442.
[72] A. Nechache, PhD Thesis, Université Pierre et Marie Curie, Paris, 2014.
[73] A. Nechache, M., Cassir, A. Ringuedé, To be published.